Mixed-Layer Budget Analysis of the Diurnal Cycle of Entrainment in Southeast Pacific Stratocumulus

PETER CALDWELL, CHRISTOPHER S. BRETHERTON, AND ROBERT WOOD

University of Washington, Seattle, Washington

(Manuscript received 22 October 2004, in final form 14 March 2005)

ABSTRACT

Mixed-layer budgets of boundary layer mass, moisture, and liquid water static energy are estimated from 6 days of data collected at 20°S, 85°W (a region of persistent stratocumulus) during the East Pacific Investigation of Climate (EPIC) stratocumulus cruise in 2001. These budgets are used to estimate a mean diurnal cycle of entrainment and, by diagnosing the fluxes of humidity and liquid water static energy necessary to maintain a mixed-layer structure, of buoyancy flux. Although the entrainment rates suggested by each of the budgets have significant uncertainty, the various methods are consistent in predicting a 6-day mean entrainment rate of 4 ± 1 mm s^{-1}, with higher values at night and very little entrainment around local noon. The diurnal cycle of buoyancy flux suggests that drizzle, while only a small term in the boundary layer moisture budget, significantly reduces subcloud buoyancy flux and may induce weak decoupling of surface and cloud-layer turbulence during the early morning hours, a structure that is maintained throughout the day by shortwave warming. Finally, the diurnal cycle of entrainment diagnosed from three recently proposed entrainment closures is found to be consistent with the observationally derived values.

1. Introduction

Marine boundary layer (BL) clouds blanket more than a quarter of the globe and are associated with a strongly negative cloud radiative forcing (Hartmann et al. 1992), felt both in the atmosphere and in the ocean. Because of this, their realistic simulation is important for modern climate modeling. The horizontal and vertical grid resolution in current climate models, however, is much too coarse to resolve the finescale processes governing these clouds, so the task is left to parameterization. Unfortunately, the interaction between stratus clouds and their environment is complex and poorly understood. As a result, current general circulation models have difficulty reproducing the current mean low cloud amount (Weare 1996) and diurnal cycle (Duynkerke and Teixeira 2001).

In the subtropics, stratocumulus-capped BLs stretch across vast regions to the west of the subtropical continents, where cool, equator-moving ocean currents meet warm, subsiding air from the Hadley circulation. The 2001 East Pacific Investigation of Climate (EPIC) stratocumulus study was designed to improve our understanding of these clouds and thus aid in their parameterization (Bretherton et al. 2004). The southeast (SE) Pacific stratocumulus region, site of the EPIC cruise, is one of the largest and most persistent area of subtropical stratus in the world (Klein and Hartmann 1993), but has received much less attention than similar areas in the Northern Hemisphere. If cloud dynamics and microphysics were similar in all regions, this neglect would not be noteworthy. Cloud condensation nuclei, however, are probably scarcer in SE Pacific stratocumulus than in similar clouds in the northeast Pacific, with as yet uncertain microphysical impacts. Additionally, the SE Pacific stratocumulus region has an unusually large and regular diurnal cycle (Rozendaal et al. 1995; Wood et al. 2002), which has a strong effect on the BL and on the surface energy balance since clouds only reflect and absorb sunlight during daylight hours. In addition, diurnal variation is an excellent test of climate models since it is an observable and reproducible response to radiative forcing (Randall et al. 2003).

A study of diurnal variation is well suited to the EPIC data, which documents a strong diurnal cycle with 3-hourly radiosonde observations and extensive remote sensing from aboard the National Oceanic and

Corresponding author address: Peter Caldwell, Department of Atmospheric Sciences, University of Washington, Box 351640, Seattle, WA 98195-1640.
E-mail: caldwep@atmos.washington.edu

Atmospheric Administration's (NOAA's) ship *Ronald H. Brown (RHB)*. In particular, we will use a 6-day "buoy period" (16–22 October 2001), during which the ship was stationed at a Woods Hole Oceanographic Institute (WHOI) buoy at 20°S, 85°W, for our analysis. Bretherton et al. (2004) summarizes the observations and initial findings from this period. Radiosondes, launched from the *RHB* every 3 h from 0200 UTC 16 October to 2300 UTC 21 October, reveal little BL stratification, with vertical gradients in liquid static energy (s_l) generally less than 2 kJ kg^{-1} and gradients in total water mixing ratio (q_t) of less than 1.5 g kg^{-1} over the BL depth of 1.2–1.4 km. Additionally, radiosonde data imply that wind shear across the BL top was minimal—the average speed shear across the layer from 50 m below to 50 m above the BL top was 0.4 m s^{-1} and the direction shear averaged 1°. Assuming the BL to be completely well mixed and shear to be negligible allows us to infer certain aspects of the diurnal cycle of turbulence. Analysis neglecting stratifying effects is commonly called the mixed-layer approximation and has a long history in the literature (Lilly 1968; Schubert et al. 1979; Bretherton and Wyant 1997). Under this approximation, turbulent mixing is assumed to dominate stratification so that thermodynamic properties closely follow adiabatic profiles (Albrecht et al. 1990; Wood and Taylor 2001). While previous studies have used this simplification primarily in modeling and theoretical work, we follow Nicholls (1984) in employing the mixed-layer assumption as a simplifying framework for deriving BL turbulent flux profiles from a limited set of observations.

This structure is helpful, because although satellite and shipboard measurements have been useful for diagnosing the diurnal cycle of some radiatively important properties of stratocumulus clouds such as cloud fraction and liquid water path (LWP), other properties such as drizzle and turbulence are more difficult to detect and as such have only been documented by a limited number of in situ studies, mostly in near-coastal regions affected by sea breezes (Brost et al. 1982; de Roode and Duynkerke 1997; Hignett 1991; Nicholls and Leighton 1986). Because stratocumulus clouds owe their existence to an intricate web of feedbacks involving surface fluxes, turbulence, large-scale subsidence, radiation, and cloud microphysics, better assessment of these difficult-to-measure quantities is essential. In a mixed-layer context, these feedbacks interact to regulate the entrainment rate (i.e., the rate of BL growth due to the incorporation of free-tropospheric air by turbulence). By controlling the growth rate of the BL and its intake of warm, dry air from the free troposphere, entrainment plays a key role in determining climatologically important parameters such as LWP and BL depth. Despite over 35 years of investigation, however, there is still controversy over how this process should be parameterized. Recent entrainment schemes vary by as much as a factor of 2 in their predictions of steady-state cloud-top height and LWP (Stevens 2002), emphasizing the need for additional observational evidence to better constraint entrainment. Thus, the main focus of this paper is to use observations taken during the EPIC cruise to provide estimates of the diurnal cycle of entrainment in the SE Pacific stratocumulus region and to assess its sensitivity to drizzle, LWP, and the inferred intensity of BL turbulence.

The remainder of the paper is divided into four sections. A derivation of the budget and flux equations used in this study is presented in section 2. The relevant data are explained in section 3. Section 4 covers the results and is followed by conclusions in section 5.

2. Methodology

a. Budget equations and entrainment rates

In this study, we focus on budgets of BL mass, heat, and moisture. The thermodynamic budgets are based on variables approximately conserved under adiabatic displacements and phase changes. The first, total water mixing ratio $q_t = q_v + q_l$, is the sum of the water vapor mixing ratio q_v and (where the air is saturated) the cloud liquid water mixing ratio q_l. The second is the liquid static energy, $s_l = c_pT + gz - Lq_l$, where T and z are temperature and height and c_p, L, and g are, respectively, the isobaric heat capacity of dry air, the latent heat of water vaporization, and the gravitational acceleration. Although c_p varies slightly with q_t and L varies slightly with T, the variations are minor, so constant values of 1004 J kg^{-1} K^{-1} and 2.5×10^6 J kg^{-1} are assumed in this study. Because the BL during EPIC was fairly deep, a vertical "pressure–height" coordinate $\hat{p} = p_0 - p$, equal to the difference between the instantaneous surface pressure p_0 and the actual pressure p, was adopted to avoid the small but quantitatively significant errors associated with a constant-density assumption. Under this framework, we arrive at horizontally and BL-averaged budget equations for q_t and s_l (derived in the appendix)

$$\hat{p}_i\left[\frac{\partial\langle q_t\rangle}{\partial t} + \langle \mathbf{v}\cdot\nabla_h q_t\rangle\right] - g\frac{\mathrm{LHF}}{L} - gF_P(0) - \hat{\omega}_e\Delta q_t = [\langle q_t\rangle - q_{t-}]\mathbf{v}\cdot\nabla_h\hat{p}_i \quad (1)$$

$$\hat{p}_i\left[\frac{\partial\langle s_l\rangle}{\partial t} + \langle \mathbf{v}\cdot\nabla_h s_l\rangle\right] - g\mathrm{SHF} + gL\cdot F_P(0) + g\Delta_{\mathrm{BL}}F_R - \hat{\omega}_e\Delta s_l = [\langle s_l\rangle - s_{l-}]\mathbf{v}\cdot\nabla_h\hat{p}_i, \quad (2)$$

TABLE 1. Mean and standard deviation (over all 6 days of sampling) for each term in the q_t budget in (1). Entrainment rates are taken from the ECMWF mass budget. Each term has been scaled into W m^{-2} for ease of comparison with the s_l budget and, with the exception of $-L\hat{p}_i/g\partial\langle q_t\rangle/\partial t$, is signed so a positive value indicates an increase in BL moisture.

	$-\frac{L\hat{p}_i}{g}\frac{\partial\langle q_t\rangle}{\partial t}$	$-\frac{L\hat{p}_i}{g}\langle\mathbf{v}\cdot\nabla_h q_t\rangle$	LHF	$LF_p(0)$	$\frac{L}{g}\hat{\omega}_e\Delta q_t$	Residual
		ECMWF/NCEP			ECMWF/NCEP	ECMWF/NCEP
Mean	−5	−26/−50	99	−5	−68/−61	−5/−22
Std dev	9	7/2	2	1	10/8	15/12

where the operator $\langle x\rangle$ denotes the mass-weighted BL average of a given quantity x, $\mathbf{v}\cdot\nabla_h x$ represents the horizontal advection of x into our layer of interest, Δx is the difference between the value of x just above the BL capping inversion and $\langle x\rangle$, and $x\_$ is the value of x just below the inversion. In addition, $F_P(\hat{p})$ (negative for downward flux) is the horizontally averaged precipitation rate at pressure–height $\hat{p}$ (in cloud, precipitation is taken to be the total liquid water flux including droplet sedimentation), and $\Delta_{\mathrm{BL}}F_R = F_R(\hat{p}_i) - F_R(0)$ is the divergence of net radiative flux (positive upward) between the BL top, $\hat{p}_i$, and the surface. The entrainment rate, w_e, is expressed here in $\hat{p}$ coordinates as $\hat{\omega}_e = \rho g\cdot w_e$ (where ρ denotes the density of air).

In an idealized mixed layer, the conserved quantities are equal to their BL-averaged value everywhere below $\hat{p}_i$, so mixed-layer analyses typically neglect the terms on the right-hand side of (1) and (2). In the present study, we have estimated the effect of these terms to always be less than 2 W m^{-2}, which is small compared to the other budget terms and to the measurement uncertainty (see Tables 1 and 2). For this reason, the rest of this paper focuses on the mixed-layer version of these equations. A schematic showing the fluxes that contribute to each mixed-layer budget is included in Fig. 1.

Using observationally derived estimates of the surface and precipitation fluxes and inferring radiative fluxes from observed thermodynamic and liquid water profiles (described in detail in section 3b), we can estimate all terms in (1) and (2) except the entrainment fluxes. Thus, estimates of $\hat{\omega}_e$ may be derived as budget residuals of (1) and (2). A third independent estimate of $\hat{\omega}_e$ may be obtained from the BL mass budget. The BL mass (given by $\hat{p}_i/g$ in the current coordinate system) changes as a result of imbalance between mass influx due to entrainment and mass outflux caused by subsidence, $\hat{\omega}_s = \partial\hat{p}_i/\partial t$. In equation form this reduces to

$$\frac{\partial\hat{p}_i}{\partial t} + \mathbf{v}\cdot\nabla_h\hat{p}_i = \hat{\omega}_e + \hat{\omega}_s. \tag{3}$$

By using radar data, satellite measurements, and large-scale gridded analyses to estimate $\partial\hat{p}_i/\partial t$, $\mathbf{v}\cdot\nabla_h\hat{p}_i$, and $\hat{\omega}_s$, respectively (all described in section 3a), we are able to diagnose $\hat{\omega}_e$ from (3). The consistency of the entrainment rates inferred from each of the three budgets is an important check on the plausibility of our results.

b. Turbulent flux profiles

1) CONSERVED-VARIABLE FLUXES

For the BL to remain well mixed, $\partial q_t/\partial t + \langle\mathbf{v}\cdot\nabla_h q_t\rangle$ and $\partial s_l/\partial t + \langle\mathbf{v}\cdot\nabla_h s_l\rangle$ must be height independent. Since the time change of a quantity at any point in space is given by the convergence of its flux function, well mixedness implies that if horizontal advection is constant in height (an assumption we make), the flux convergence of q_t and s_l must be constant in height, or equivalently, that these fluxes must themselves be linear functions of $\hat{p}$. In terms of our mixed-layer budgets, the flux function for q_t is

$$W(\hat{p}) = \overline{\hat{\omega}' q_t'} + gF_P(\hat{p}), \tag{4}$$

and for s_l it is

$$E(\hat{p}) = \overline{\hat{\omega}' s_l'} + g[F_R(\hat{p}) - L\cdot F_P(\hat{p})]. \tag{5}$$

TABLE 2. Same as Table 1, but for the s_l budget in (2).

	$-\frac{\hat{p}_i}{g}\frac{\partial\langle s_l\rangle}{\partial t}$	$-\frac{\hat{p}_i}{g}\langle\mathbf{v}\cdot\nabla_h S_l\rangle$	SHF	$-LF_p(0)$	$-\Delta_{\mathrm{BL}}F_{\mathrm{SW}}$	$-\Delta_{\mathrm{BL}}F_{\mathrm{LW}}$	$\frac{1}{g}\hat{\omega}_e\Delta s_l$	Residual
		ECMWF/NCEP					ECMWF/NCEP	ECMWF/NCEP
Mean	0	−19/−20	14	5	26	−78	41/38	11/6
Std dev	3	3/1	1	1	1	1	6/5	8/6

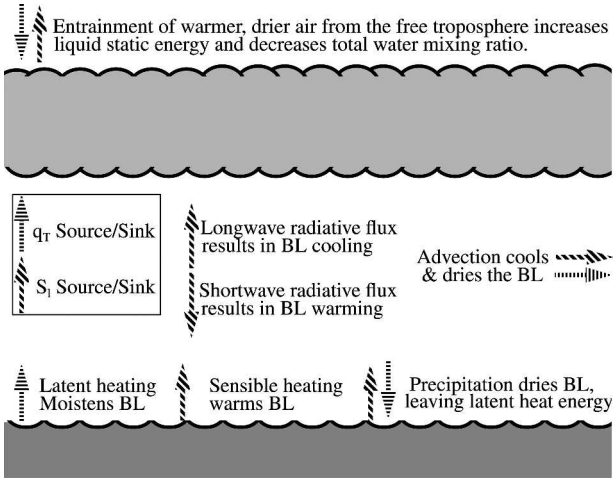

FIG. 1. Schematic of BL indicating sources and sinks of $\overline{q_t}$ and $\overline{s_l}$.

In these equations, positive flux indicates upward transport, the overbar is used to emphasize the horizontal averaging process, and primes denote perturbations from this average. If (4) and (5) vary linearly with $\hat{p}$, $W(\hat{p})$ and $E(\hat{p})$ are uniquely determined by their surface and cloud-top values so

$$W(\hat{p}) = g\left[\frac{\text{LHF}}{L} + F_P(0)\right]\left(1 - \frac{\hat{p}}{\hat{p}_i}\right) - \hat{\omega}_e \Delta q_t \frac{\hat{p}}{\hat{p}_i}, \quad (6)$$

$$E(\hat{p}) = g[\text{SHF} - LF_P(0) + F_R(0)]\left(1 - \frac{\hat{p}}{\hat{p}_i}\right) + [gF_R(\hat{p}_i) - \hat{\omega}_e \Delta s_l]\frac{\hat{p}}{\hat{p}_i}. \quad (7)$$

By substituting (6) and (7) into (4) and (5) and solving for the corresponding turbulent fluxes, equations for the turbulent flux profiles of q_t and s_l may be obtained.

2) BUOYANCY FLUXES AND CONVECTIVE VELOCITY

For a subtropical stratocumulus-capped BL with negligible wind shear, the main source of turbulent kinetic energy is buoyancy flux:

$$\mathcal{B} = \frac{1}{\rho s_{v0}} \overline{\hat{\omega}' s_v'}. \quad (8)$$

Here, the virtual static energy $s_v = c_p T_v + gz$ is defined in terms of virtual or "density" temperature (including liquid loading) $T_v = T + T_{\text{ref}}(\delta q_v - q_l)$, where $\delta = 0.608$ and $T_{\text{ref}} = 290$ K. The term s_{v0} is a reference virtual static energy (taken here to be 290 kJ kg^{-1}—the mean over all soundings of s_v at 50 mb).

We now relate $\mathcal{B}$ to the conserved variable fluxes following Bretherton and Wyant (1997) but working in terms of liquid static energy rather than moist static energy. Using the definition $s_l = c_p T + gz - Lq_l$, s_v may be rewritten as

$$s_v = s_l + (1 - \varepsilon)Lq_l + \delta\varepsilon Lq_v, \quad (9)$$

where $\varepsilon = c_p T_{\text{ref}}/L \approx 0.1$. Expressing this quantity in terms of the conserved variables is particularly simple below cloud base, as $q_l = 0$ and thus $q_v = q_t$. Within the cloud, q_v is assumed equal to the saturation mixing ratio, q_{sat}, so that

$$q_v' = \frac{\partial q_{\text{sat}}}{\partial T} T' = \frac{1}{c_p}\frac{\partial q_{\text{sat}}}{\partial T}[s_l' - L(q_t' - q_v')].$$

Solving this last equation for q_v' and setting $\gamma = (L/c_p)(\partial q_{\text{sat}}/\partial T)$, we can express (9) in terms of s_l' and q_t' in the cloud layer. Together, the subcloud and in-cloud forms of (9) imply

$$\overline{\hat{\omega} s_v'} = \begin{cases} \overline{\hat{\omega}' s_l'} + \delta\varepsilon L\overline{\hat{\omega}' q_t'}, & 0 \le \hat{p} < \hat{p}_{\text{cb}} \\ \beta\overline{\hat{\omega}' s_l'} + (\beta - \varepsilon)\overline{L\hat{\omega}' q_t'}, & \hat{p}_{\text{cb}} < \hat{p} < \hat{p}_i \end{cases}. \quad (10)$$

Here, $\hat{p}_{\text{cb}}$ is the cloud-base pressure–height and $\beta = [1 + \varepsilon\gamma(\delta + 1)]/(\gamma + 1) \approx 0.5$ is a weak function of pressure and temperature (Randall 1980). In section 4c, mixed-layer buoyancy flux profiles constructed by applying the data described in section 3 to Eq. (10) are discussed.

The convective velocity scale, w_*, a measure of the overturning velocity of buoyantly driven eddies, is then calculated as

$$w_* = \left[2.5\frac{z_i}{\hat{p}_i}\int_0^{\hat{p}_i} \mathcal{B}\, d\hat{p}\right]^{(1/3)}, \quad (11)$$

where z_i is the BL depth expressed in meters. Here, we have adapted the standard definition of w_* (e.g., Nicholls and Turton 1986) to $\hat{p}$ coordinates based on the derivation of a turbulent kinetic energy equation from the same governing equations in $\hat{p}$ coordinates used to derive (1) and (2). This equation is important for the entrainment parameterizations tested in section 4d.

3. Data

a. Mass budget

We assume (consistent with soundings) that cloud top always coincides with inversion base. Thus entrainment may be calculated from (3) by combining measurements of cloud-top-height tendency, subsidence

rate, and advection of cloud-top height. During the cruise, measurements of cloud-top height were obtained at 15-s resolution from a vertically pointing 35-GHz cloud radar. These data were averaged into 3-h means with the first mean centered at 0200 UTC 16 October; $\partial \hat{p}_i/\partial t$ was then approximated using centered differencing. Estimates of subsidence rate at the buoy location were obtained from 12- to 35-h forecasts (obtained at full-model vertical resolution) by both the European Centre for Medium-Range Weather Forecasts (ECMWF) operational forecast model (courtesy of M. Köhler at ECMWF) and the National Centers for Environmental Prediction (NCEP) medium-range forecast model (courtesy of H.-L. Pan at NCEP and S. Krueger at the University of Utah). These models assimilated surface meteorological data from the WHOI buoy but not from the *RHB* radiosonde soundings described in the next section. McNoldy et al. (2004) showed that, at least on climatological time scales, subsidence from reanalysis versions of these models is in good agreement with QuikSCAT data. Advection of inversion height is assumed to have a constant value of -0.49 mm s^{-1}, diagnosed as the large-scale slope of satellite-derived cloud-top height based on a climatology from October to November 2000, which is a comparable season (Wood and Bretherton 2004). We chose this estimate despite probable synoptic and diurnal variations in the advection of inversion height, noting that because its climatological mean value is an order of magnitude smaller than the other budget terms, exact diagnosis of cloud-top-height advection is probably not quantitatively important to the mass budget.

b. Moisture and liquid static energy budgets

For our budgets, we compute BL-averaged q_t and s_l from the radiosonde profiles at each launch time as the mean of the profile over the layer from 50 m above the surface to the base of the inversion capping the BL. The 50-m lower limit was chosen to avoid errors associated with ship deck heating. The inversion base was chosen by eye as the height at which q_t begins to drop from relatively large BL values (typically 8 g kg^{-1}) to the extremely dry values found in the overlying air (usually 2 g kg^{-1} or less, see Fig. 3). This measure of inversion base agrees reasonably well with the radar-derived value; the root-mean-square error between the two versions is 64 m and the sonde-based $\hat{p}_i$ is 35 m lower on average (the diurnal cycle of these two quantities is compared in Fig. 9). The q_t and s_l profiles are computed by combining radiosonde-derived measurements of q_v and T with estimates of q_l. A q_l profile was estimated for each 3-h period by assuming liquid water content increases linearly from a cloud-base value of zero to a cloud-top value such that $1/g \int_{\hat{p}_b}^{\hat{p}_i} q_l \, d\hat{p}$ matches the observed liquid water path. Liquid water path was obtained at 5-min resolution from a NOAA shipboard microwave radiometer following Hogg et al. (1983). This quantity, and all others obtained at higher-than-radiosonde resolution, was averaged into 3-h means centered on the radiosonde launch times. One exception, however, is cloud base, which was obtained at 15-s resolution from the NOAA/Environmental Technology Laboratory (ETL) ceilometer. The lowest altitude return was composited into hourly median values before averaging into 3-h means about the radiosonde launch times. This added complexity was introduced to avoid bias introduced by large outliers in the apparent cloud base that we believe was a ceilometer response to intermittent subcloud drizzle. Cloud fraction was taken to be the fraction of each 3-h period that the ceilometer registered a cloud base. Density is derived from the ideal gas law. Time derivatives of $\langle q_t \rangle$ and $\langle s_l \rangle$ are computed using centered differencing. Advective terms are estimated from the ECMWF and NCEP forecasts mentioned in section 3a. Results from both models are compared in section 4.

Surface sensible and latent heat fluxes are derived from temperature and humidity measurements taken on the *RHB* instrumented tower (14-m altitude) using the bulk flux algorithm described by Fairall et al. (1996), who estimated the error in these fluxes to be less than 5 W m^{-2}. The fluxes agreed to within this accuracy with similarly derived fluxes from buoy measurements when the ship and buoy were collocated. Cloud-base precipitation averaged over a 30-km radius centered on the ship was diagnosed from C-band radar, then expanded into below-cloud precipitation flux profiles by a sedimentation/evaporation model based on theoretical reflectivity profiles generated using ETL's millimeter-wavelength vertically pointing radar on the *RHB* as described in detail by Comstock et al. (2004). In cloud, a constant precipitation rate equal to the value at cloud base is assumed. This approximation was suggested in Nicholls (1984) based on observational data showing that the increase toward cloud base in the precipitation rate for rain drops and the increase toward cloud top in the sedimentation rate for cloud droplets roughly cancel each other, resulting in a fairly constant precipitation flux throughout the cloud layer (since precipitation is taken in this study to be synonomous with total liquid water flux). Radiative fluxes are computed by BUGSrad, a two-stream correlated-k radiative transfer scheme developed at Colorado State University (Stephens et al. 2001). Both satellite and cloud radar observations did not detect any cloud above the BL over the *RHB* during the 6-day period. To obtain real-

istic fluxes for partly cloudy conditions, results from clear- and cloudy-sky radiative transfer calculations were combined in an average that was weighted by the ceilometer-derived cloud fraction. The liquid water profile for purely cloudy conditions was taken to be the previously calculated q_l profile divided by the cloud fraction in order to account for the fact that the observed LWP was an average value of both cloudy and clear conditions. To overcome the lack of radiosonde data at higher altitudes, missing profile data below 15 km were interpolated from neighboring profiles, and above 15 km all profiles were blended into the McClatchey et al. (1972) standard tropical atmospheric profiles. Droplet number concentrations N_d were provided by C. Fairall at NOAA/ETL. As discussed by Bretherton et al. (2004), this quantity was estimated during daylight hours from simultaneous measurements of cloud thickness, LWP, and cloud optical depth following Dong and Mace (2003). Nighttime values were then generated by linear interpolation. Effective radius r_e was calculated using the parameterization of Martin et al. (1994),

$$r_e = \left[\frac{3\rho q_l}{4\pi\rho_w k N_d}\right]^{(1/3)}, \tag{12}$$

where $k = 0.8$ (as suggested for clean air) and ρ_w is the density of water. Droplet concentrations during EPIC ranged from 50 to 160 droplets cm^{-3}, resulting in cloud-top effective radii of 8 to 18 μm.

Comparison between calculated and observed downwelling radiative fluxes at the surface (Fig. 2) shows our approach to slightly underestimate surface shortwave fluxes, although comparison with simultaneous observations from the WHOI buoy (included as triangular and circular points) suggests that the magnitude of the error induced by this bias is comparable to the sampling uncertainty. Triangular markers denote times when the ship and buoy were collocated, thus they serve as a strict measure of instrument calibration uncertainty. Circular markers indicate times when the ship was away from the buoy (typically by less than 20 km) and thus show the effect of mesoscale variability on radiative fluxes. Since our radiative profiles are derived from a single sounding while the shipboard radiometer data are averaged over 3 h, it is unsurprising that the disagreement between the derived fluxes and the shipboard observations is of similar magnitude to that shown by the circular markers. Although the differences between ship observations and radiative transfer calculations are sometimes quite large, it is important to remember that our budgets depend only on the flux actually absorbed in the BL. Because the BL absorbs only a small fraction of the impinging solar radiation, errors in the BL net shortwave flux divergence can be expected to be much less than errors in the surface downwelling solar radiation. Calculated longwave fluxes agree quite well with the observations, with perhaps a 5 W m^{-2} high bias for lower fluxes (e.g., decreased cloudiness).

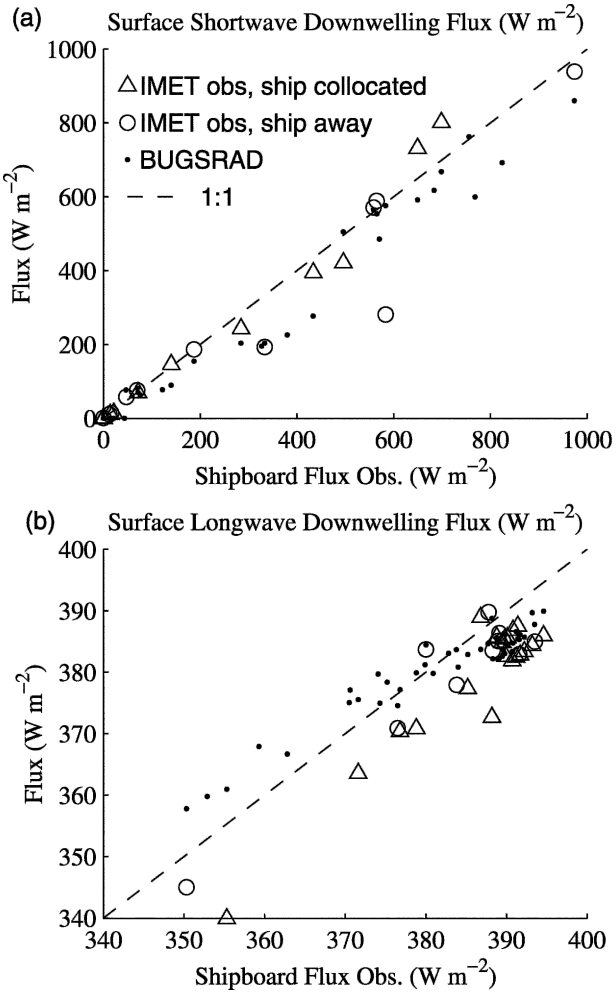

FIG. 2. Comparison of observed downwelling flux at the surface with values calculated using the BUGSrad scheme. Coincident observations from the IMET buoy are included where available. Observations made when the RHB is located at the buoy are indicated by triangles. Values when the *RHB* is located near but not at the buoy are also included as circles.

c. Cross-inversion jumps

A practical complication of imposing a mixed-layer idealization on any real BL is how to optimally determine inversion jumps. An issue during EPIC was apparent systematic errors in radiosonde-derived temperature profiles just above the inversion. Figure 3 compares the q_v and T soundings from a typical radio-

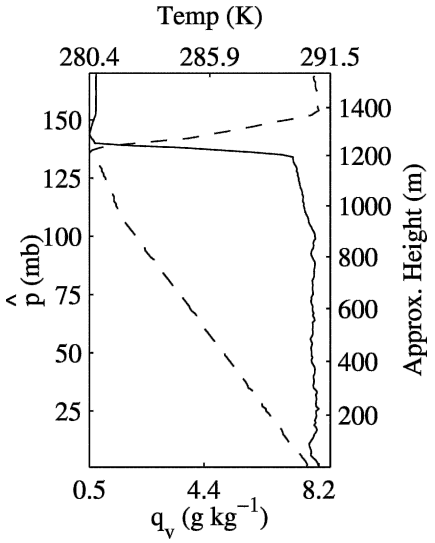

FIG. 3. Mixing ratio (solid line) and temperature (dashed line) profiles from the radiosonde launched at 0200 UTC (2000 LT) on 16 Oct 2001. The temperature inversion appears to be around 15 mb (≈150 m) deep, which is 5 times as thick as the moisture inversion.

sonde launch, 0200 UTC 16 October. In this figure, the inversion thickness diagnosed from the q_v sounding is around 3 mb (~30 m, i.e., a value consistent with the literature; Caughey et al. 1982; Lenschow et al. 2000). The T sounding, on the other hand, includes a 15-mb (~150 m) layer where T increases with height, rather than a jumplike inversion. The reason for this thick temperature inversion is still unclear. One possibility we have investigated is that the broad temperature inversion is a real response to enhanced radiative cooling in the air just above cloud top. This conclusion is inconsistent, however, with the radiative cooling profile in Fig. 4a, which shows that the region just above the cloud top is so cold that radiative transfer should be warming this region. Error due to the temperature-sensor lag was also considered, but could not explain the nearly linear increase in temperature over such a deep layer. One possibility that we could not discredit is that cloud droplets wet the sensor as it passes through cloud, and subsequently interfere with sensor response above the cloud through evaporative cooling. Radiosonde inaccuracy in stratocumulus inversions have not, to our knowledge, been documented in other studies, a fact that is perhaps unsurprising because radiosondes have not previously been used to scrutinize the precise vertical structure above the cloud in the presence of such strong inversions. Comparison of radiosonde data with simultaneous aircraft/dropsonde measurements, use of tethered balloons, or performance of laboratory experiments quantifying the effect of wetting on radiosonde temperature sensors would be useful for investigating the cause of this problem.

To avoid using temperature measurements in this uncertain region to compute cross-inversion jumps, we infer s_l at the top of the BL from its value some distance above. To account for the radiative cooling taking place as air subsides from the height where it is measured to the height at which it is entrained, a correction offset is applied. Ideally, this offset would depend on the time-

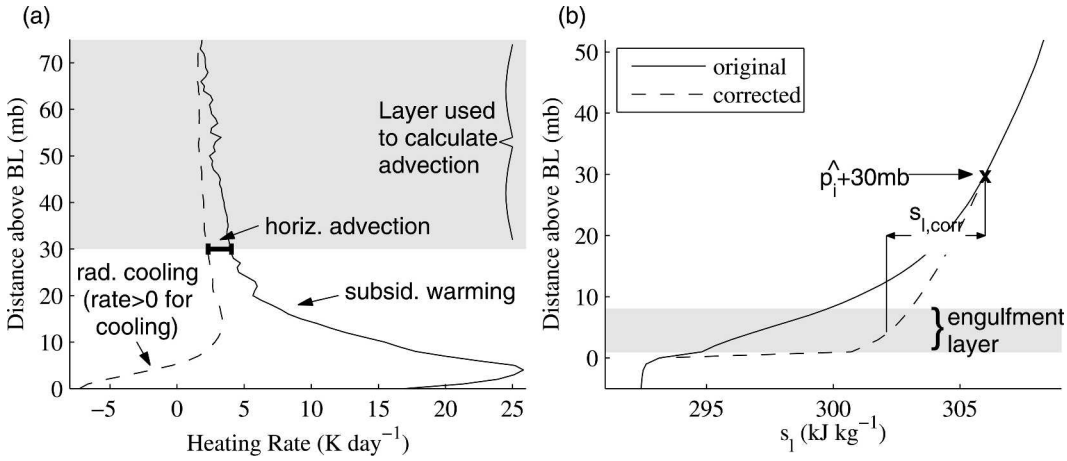

FIG. 4. (a) Heating rate due to subsidence warming (solid lines, positive numbers indicate warming) and radiative cooling (dashed lines, positive numbers correspond to cooling). The layer used to calculate advection is indicated in the upper-right-hand corner. In this region, the difference between subsidence warming and radiative cooling is interpreted as the advective tendency. A linear fit to this difference is used to diagnose advection in the region between this layer and the cloud top. (b) The uncorrected (solid) and corrected (dashed) s_l profiles along with a diagrammatic description of the engulfment layer.

varying entrainment rate and the above-inversion moisture profile, among other quantities difficult to assess from the available data. After discovering that more sophisticated approaches all occasionally predicted unreasonably large corrections due to this uncertainty, we applied a single correction to all soundings. This correction is derived by considering the evolution of s_l in the layer above the inversion base. Because this layer is defined relative to $\hat{p}_i$, switching to a cloud-top-relative coordinate system (with vertical coordinate $\zeta = \hat{p} - \hat{p}_i$) simplifies the analysis. In this context,

$$\frac{\partial s_l}{\partial t} + \mathbf{v} \cdot \nabla_h s_l - \hat{\omega}_e \frac{\partial s_l}{\partial \zeta} = -g \frac{\partial F_R}{\partial \zeta}, \qquad (13)$$

where the horizontal gradient is taken here along a surface of constant ζ. Note that air above the BL is moving toward $\hat{p}_i$ at a rate $\hat{\omega}_s - (\partial \hat{p}_i/\partial t + \mathbf{v} \cdot \nabla_h \hat{p}_i)$, which, taking $\hat{\omega}_s$ to be constant over the depth of the shallow correction region and applying (3), is equal to $-\hat{\omega}_e$.

Averaged over the 6-day period, the soundings imply that $\partial s_l/\partial t$ is negligible. Thus (13) reduces to a balance between horizontal advection, subsidence warming and radiative cooling. Corrections to the 6-day mean s_l profile just above the cloud top were made by forcing the s_l profile in the lowest 30 mb above the inversion to obey this balance by running (13) to equilibrium holding all other thermodynamic quantities fixed and using upstream differencing to resolve the sharp gradient at the cloud top. In this calculation, radiative fluxes were derived using the BUGSrad scheme and a daily-mean zenith angle of 71° was applied. Thermodynamic profiles were computed by rescaling the individual profiles at each time to have $\hat{p}_i$ equal to the mean inversion height over all soundings, then temporally averaging to create 6-day mean profiles with a sharp inversion. An $\hat{\omega}_e$ value of 3.5 mm s^{-1} was used for this calculation. This value is derived in section 4a using the mass budget (3) with ECMWF subsidence, which we show in 4b to be consistent with similar measures from the 6-day mean BL s_l and q_t budgets. We diagnose the vertical profile of advection in the correction region by extrapolating trusted advection values from above the correction region downward. These trusted $\mathbf{v} \cdot \nabla_h s_l$ values are diagnosed as the residual of (13) with $\partial s_l/\partial t = 0$. This residual, presented in Fig. 4a as the difference between subsidence warming and radiative cooling, appears to decrease linearly with height above about $\hat{p}_i$ + 30 mb. Based on this observation, we approximate horizontal advection by a linear least squares fit to the subsidence warming/radiative cooling residual in the region topping the inversion by 30–75 mb. This process results in a horizontal advection tendency given by

$$\mathbf{v} \cdot \nabla_h s_l = 8.5 \times 10^{-2} - 3.78 \times 10^{-4} \cdot \hat{p}. \qquad (14)$$

Just above the inversion, this method suggests an s_l advection of 2.8 kJ kg^{-1} day^{-1}. Because this measure of advection ceases to match the predictions of Fig. 4a below $\hat{p}_i$ + 30 mb, we choose our correction layer to extend from the inversion base to this level. The depth of this layer also happens to be the distance a typical air parcel will subside in a day, so correcting over this depth has the added advantage that it facilitates using an entrainment rate that has been averaged over the diurnal cycle and is therefore more robust.

By substituting the advection derived from (14) into (13) and running (13) to equilibrium using upstream differencing, a corrected s_l profile may be generated. This profile is presented in Fig. 4b. Comparison of the original and corrected s_l profiles serves as a further illustration of how out of balance the uncorrected profiles were. Also indicated in this graphic is the engulfment layer (i.e., the region from which air is typically entrained). The depth of this layer is a rather uncertain quantity; we take the engulfment layer depth to be 8 mb based on recent analysis from aircraft flights in the California stratus region by Faloona et al. (2005) and estimate the liquid static energy of entrained air to be the mean value of the corrected s_l profile over this layer. Application of this definition to Fig. 4b implies that if we want to estimate s_l in the entrainment layer based on its value 30 mb above, we must apply a correction $s_{l,\mathrm{corr}}$ of −4.0 kJ kg^{-1} to $s_l|_{\hat{p}_i+30\,\mathrm{mb}}$. Conceptually, this correction amounts to the radiative cooling occurring as air descends to the BL from 30 mb above. In the absence of a reliable time-varying correction, we simply assume that $\Delta s_l = (s_l|_{\hat{p}_i+30\,\mathrm{mb}} - 4.0\ \mathrm{kJ\ kg^{-1}} - \langle s_l \rangle)$ for each sounding.

One of our main motivations for examining the s_l budget is to derive entrainment rates from (2). In fact, it was the examination of uncorrected s_l budget entrainment rates (which average an implausible 15 mm s^{-1} when $\Delta s_l = s_l|_{\hat{p}_i+3\,\mathrm{mb}} - \langle s_l \rangle$) that provided our first indication of temperature sounding errors. Because we use the agreement between entrainment rates derived from the various budgets as an indicator of the uncertainty in our best-guess entrainment predictions, it is important to examine the sensitivity of the s_l budget entrainment rates to an error in our correction scheme. Propagation of error through (2) reveals that a fractional error in $s_{l,\mathrm{corr}}$ will induce an error $s_{l,\mathrm{corr}}/\Delta s_l \approx 0.4$ times as large in $\hat{\omega}_e$. Since $s_{l,\mathrm{corr}}$ is an intuitively reasonable amount of cooling to occur at the top of the BL over the course of a day, error in this quantity is probably less than 25%, resulting in an entrainment uncertainty of a magnitude comparable to other terms in the

budgets. Applying similar analysis to w_*^3, it appears that errors in $s_{l,\mathrm{corr}}$ induce errors of roughly equal size in w_*^3. Because w_* is calculated through (8), which is technically only valid under idealized mixed-layer conditions, uncertainty in $s_{l,\mathrm{corr}}$ is probably not the leading source of error in this calculation either. Further, applying perturbations to $s_{l,\mathrm{corr}}$ does not seem to have a strong impact on the performance of the entrainment parameterizations considered in section 4d.

In an effort to avoid problems associated with variations in inversion depth, above-inversion total water mixing ratio is sampled at 10 mb above the BL. Because q_t varies little with height just above the BL (e.g., see Fig. 3), this value is used in Δq_t without adjustment.

4. Results

a. Entrainment from the mass budget

Figure 5 presents the diurnal cycles of $\hat{\omega}_s$, $\partial\hat{p}_i/\partial t$, and $\hat{\omega}_e$ [calculated as a budget residual of (3) using $\hat{\omega}_s$, $\partial\hat{p}_i/\partial t$, and the assumed horizontal advective inversion-height tendency]. Both ECMWF and NCEP analyses of $\hat{\omega}_s$ suggest a large diurnal cycle of subsidence, peaking around midday and damping to zero around midnight, although the NCEP analyses are noisier and have a larger semidiurnal component. The large amplitude of this cycle is associated with a gravity wave driven by daytime heating on the Andean slopes 1500 km away (Garreaud and Muñoz 2004). This causes a rapid increase in BL thickness at night ($\partial\hat{p}_i/\partial t > 0$) and decrease in BL thickness during the day ($\partial\hat{p}_i/\partial t < 0$). With either analysis, the diurnal cycle of $\hat{\omega}_e$ is qualitatively in accord with expectation for radiatively driven stratocumulus. The implied entrainment rate is large at night ($\hat{\omega}_e = 5 \times 10^{-4}$ mb s^{-1}, or approximately 5 mm s^{-1}) and drops to zero near local noon when cloud heating due to solar absorption could be expected to be largest and most effective at suppressing in-cloud turbulence. The ECMWF results are more believable, since NCEP analysis implies significantly negative midday entrainment, which is physically implausible. Additionally, the ECMWF-implied $\hat{\omega}_e$ is quasi steady throughout the night, which matches expectations since longwave radiative forcing is essentially steady and large during this time. Nonetheless, the discrepancy between ECMWF and NCEP subsidence rates can be taken as a measure of the uncertainty in this quantity. The average entrainment rates for the 6 days of study are 3.5 and 3.2 mm s^{-1} based on the ECMWF and NCEP analyses, respectively. Estimating $\hat{p}_i$ from the moisture inversion (as done for the q_t and s_l budgets) results in entrainment rates just 0.1 mm s^{-1} higher in the mean and negligibly different in the diurnal cycle, which suggests that variation in $\partial\hat{p}_i/\partial t$ are not a large source of error in this study. The 6-day mean entrainment rates calculated from the mass budget compare well with the climatological value of just over 3 mm s^{-1} value obtained by Wood and Bretherton (2004).

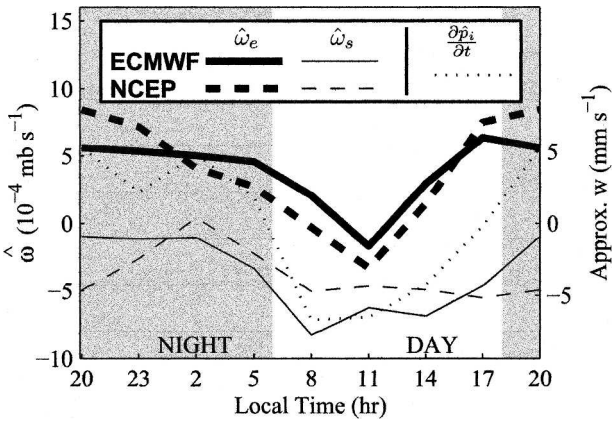

FIG. 5. Diurnal cycle of entrainment as diagnosed from the BL mass budget. Entrainment rates are denoted by thick lines, subsidence rates by thin lines, and sonde-derived BL height tendency by dots. ECMWF values are presented in unbroken lines, while NCEP values are dashed.

b. Analysis of the q_t and s_l budgets

1) THE 6-DAY MEAN

Each term in the mixed-layer moisture and energy budgets (1) and (2) was estimated at each radiosonde launch time using the data described in section 3. The resulting time series were averaged into 6-day means, which are presented in Tables 1 and 2. All terms are given in energy flux units for consistency. The entrainment rates are inferred from the mass budgets. In both budgets there are balances between dominant terms. Table 1 reveals that surface evaporation is balanced primarily by entrainment drying and secondarily by horizontal dry advection. The s_l budget, on the other hand, indicates that longwave cooling and (to a lesser extent) cold advection balance comparable contributions from entrainment, shortwave warming, and sensible heating. Precipitation does not play a significant role in either budget. Although significant cloud-base drizzle was observed on several of the study days, a high cloud base (ranging from 800 to 1100 m) meant that almost all precipitation evaporated before reaching the surface (Bretherton et al. 2004; Comstock et al. 2004). Wood (2004, manuscript submitted to *J. Atmos. Sci.*) suggests that the EPIC case is not unusual in this regard and that in general, drizzle tends to largely evaporate before reaching the surface below stratocumulus clouds with bases higher than 500 m.

In each table, an estimate of the sampling uncertainty for the 6-day mean is given as

$$\sigma_{\text{mean}} = \sqrt{\frac{1}{48}\left[\frac{1}{8}\sum_{k=1}^{8}\sigma_k^2\right]}, \tag{15}$$

where σ_k is the standard deviation of the data at the kth time of day. In using this measure, we assume that error is independent of time of day, so our best guess as to the standard deviation at any point in the dataset is $\frac{1}{8}\sum_{k=1}^{8}\sigma_k^2$. Under these assumptions, (15) is the standard deviation in the 6-day mean. It is important to realize that this error statistic reflects only sampling variability and does not capture biases due to calibration error or to uncertainties in the analysis methods. Additionally, much of σ_k could be due to real synoptic variability rather than an inability to accurately sample quantities at individual times. In this case σ_{mean} may have little to do with the accuracy of a budget term, instead reflecting its representativeness as a longer-term mean to the extent this can be assessed from only 6 days of data. From this perspective, however, σ_k is only a lower bound, since synoptic variations are autocorrelated over periods of several days. In spite of these caveats, we will interpret σ_{mean} for individual budget terms as a rough guide to the representativeness of the balances in our 6-day mean. Taken in this context, the tendencies of both q_t and s_l in the 6-day mean are not significantly different than zero, which is encouraging since time invariance suggests that the averages captured here are representative of a longer-term mean rather than of only our particular 6 days of data. Another indication of useful budgets is that the sampling variability of all remaining budget terms is reassuringly small compared to the magnitude of their mean values.

A second, more robust measure of the uncertainty inherent in the budget calculations is available in the form of 6-day mean budget residuals. It is in assessing these residuals that our error analysis is most compelling, because this error really does reflect sampling inadequacy or biases. These residuals are presented in the last columns of Tables 1 and 2. That the budgets generally do not close to within the calculated uncertainties illustrates that standard error analysis tends to underpredict the actual error in this type of study.

We saw in Fig. 5 that estimation of the time series of subsidence at a remote ocean location from model analyses may be subject to large systematic errors that may depend on the diurnal cycle. These errors may affect the mass budget estimate of entrainment. Hence, another perspective on the heat and moisture budgets is as a way to get independent estimates of $\hat{\omega}_e$ by solving for the entrainment fluxes as budget residuals in (1) and (2). Applied in this way, the q_t budget yields a 6-day mean entrainment rate of 4.3 mm s^{-1}, while the s_l budget yields 4.7 mm s^{-1}. Comparison of the three independent entrainment estimates for this period suggests a mean entrainment rate for the buoy period of roughly 4 ± 1 mm s^{-1}.

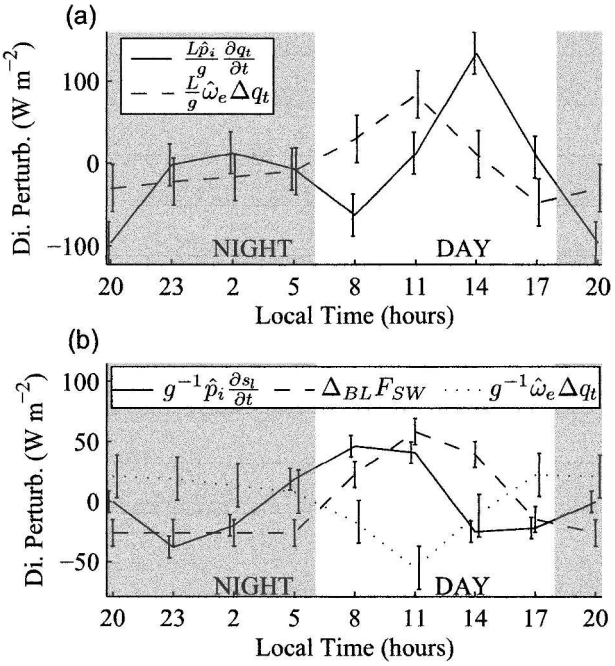

FIG. 6. Diurnal cycle for budget terms with large diurnal amplitude (omitted terms have diurnal cycles of 10 W m^{-2} or less). For ease of comparison, means have been removed from each term and the sign convention is such that a positive perturbation increases q_t or s_l. Error bars represent standard deviations in the mean for each time of day (as described in the text).

2) DIURNAL CYCLE

Only a few terms in the q_t and s_l budgets have diurnal cycles of significant amplitude. These terms are plotted in Fig. 6 (with entrainment fluxes based on $\hat{\omega}_e$ from the ECMWF mass budget and signs chosen so that a positive perturbation increases q_t or s_l). In the moisture budget, decreased entrainment drying during the day results in a buildup of BL moisture, which is then depleted by more vigorous entrainment at night. The diurnal cycle of liquid static energy involves an increase in $\langle s_l \rangle$ during the day due to solar heating, followed by a decrease after sunset that is partially mitigated by enhanced entrainment of warm air from the free troposphere at night.

An estimate of the sampling variability involved in these calculations is made following (15). Day-to-day variability in storage ($=\hat{p}_i\partial/\partial t$ i.e., the rate at which a

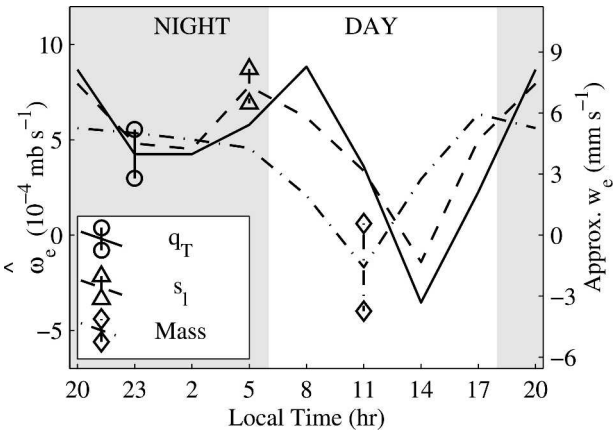

FIG. 7. Comparison of the diurnal cycle of entrainment as calculate d from the q_t budget (solid lines, circular endpoints on error bar), from the s_l budget (dashed lines, triangular endpoint), and from the subsidence method (dot–dashed lines, diamond endpoint). Error bars represent one standard deviation limits on the mean associated with sample variability over the 6 days. Only one error bar is presented for each method because the error is assumed identical for each time of day.

quantity accumulates in the BL) and entrainment warming/drying are assumed to be independent of time of day, so the error in these quantities should be $\sigma_{di} = \sqrt{8}\sigma_{\text{mean}}$ since there are 8 times fewer samples for each time of day than for the mean. Shortwave heating—important in the s_l budget—has zero variability at night, rendering (15) inappropriate. Instead, the error bars given on $\mathbf{\Delta}_{\text{BL}}F_{\text{SW}}$ during the daytime are taken as the standard deviation of the data at that time of day.

By deriving entrainment fluxes for each time of day as residuals of (1) and (2), we are able to infer time series of entrainment, which are shown in Fig. 7 with error bounds again calculated as $\sqrt{8}\sigma_{\text{mean}}$. The estimates are broadly consistent with the subsidence-based entrainment prediction, with a nocturnal maximum of approximately 5 mm s^{-1} and a sharp drop toward midday. Both estimates predict the $\hat{\omega}_e$ minimum to occur later than suggested by the subsidence budget. Again, the error bounds provide only a rough measure of sample variability, although evidence of systematic bias is present as well. For example, the q_t budget suggests negative entrainment around midday, which is clearly unphysical. Additionally, confidence bounds in Fig. 7 are disjoint for some methods at some times of day. Comparing Fig. 7 to Fig. 6, we see that our estimates of the diurnal cycle of entrainment from the q_t and s_l budgets are largely modulated by the diagnosed diurnal cycle of storage, which is one of the more uncertain measurements in the budgets because it is based on a single radiosonde profile every 3 h. Nonetheless, all three budgets yield a similar diurnal profile and mean value of w_e, which increases our confidence in the entrainment estimates from the individual budgets. For the remainder of this paper, ECMWF mass budget entrainment rates will be used wherever entrainment observations are required.

c. Diurnal cycle of turbulence

Using the method described in section 2b, buoyancy flux profiles were calculated for each 3-h interval. Where possible, the data used in this calculation are presented in Table 3. Because calculation of the turbulent fluxes depends strongly on the mixed-layer assumption, we emphasize that when the BL is not well mixed, our method of inferring buoyancy flux becomes inappropriate.

Figure 8a shows the 6-day mean diurnal cycle of mixed-layer inferred buoyancy flux. At all times of day, the profiles have the structure expected of a radiatively driven cloud-topped mixed layer—small values near the surface decreasing to a minimum at cloud base, then jumping up to reach a maximum value in the cloud. Also apparent is a diurnal cycle in the intensity of buoyancy flux within the cloud. The nighttime maximum is

TABLE 3. Quantities useful for the calculation of $\mathcal{B}$ or for testing parameterizations. Entrainment rates are taken from the ECMWF mass budget, which predict the entrainment value denoted by 0* to be less than zero; a value of zero is assumed for this study.

Time (LT)	$\hat{p}_b$ (mb)	$\hat{p}_i$ (mb)	$q_l\|_{\hat{p}_i}$ (g kg^{-1})	Δq_t (g kg^{-1})	Δs_l (kJ kg^{-1})	$\hat{\omega}_e$ (Pa s^{-1})	$F_p(0)$ (kg m^{-2} s^{-1})	$F_p(\hat{p}_b)$ (kg m^{-2} s^{-1})	$\Delta_{\text{BL}}F_R$ (W m^{-2})	SHF (W m^{-2})	LHF (W m^{-2})	w_* (m s^{-1})
0200	102	141	0.71	−6.81	10.77	5.0×10^{-2}	-4.5×10^{-6}	-1.4×10^{-5}	79	17	108	1.19
0500	108	151	0.71	−6.68	10.55	4.6×10^{-2}	-5.0×10^{-6}	-1.9×10^{-5}	78	17	105	1.12
0800	107	146	0.61	−6.07	10.90	2.1×10^{-2}	-2.7×10^{-6}	-1.2×10^{-5}	29	17	102	0.88
1100	109	135	0.48	−6.33	10.34	0*	-7.0×10^{-7}	-3.5×10^{-6}	−8	15	97	0.91
1400	104	130	0.42	−6.86	9.72	2.9×10^{-2}	-2.8×10^{-7}	-2.3×10^{-6}	11	13	87	0.90
1700	101	125	0.66	−6.61	9.27	6.4×10^{-2}	-4.5×10^{-7}	-3.3×10^{-6}	66	11	92	1.07
2000	104	136	0.52	−6.70	10.59	5.6×10^{-2}	-1.4×10^{-6}	-5.8×10^{-6}	79	11	97	1.20
2300	103	140	0.73	−6.52	10.93	5.4×10^{-2}	-1.2×10^{-6}	-4.7×10^{-6}	80	12	102	1.18

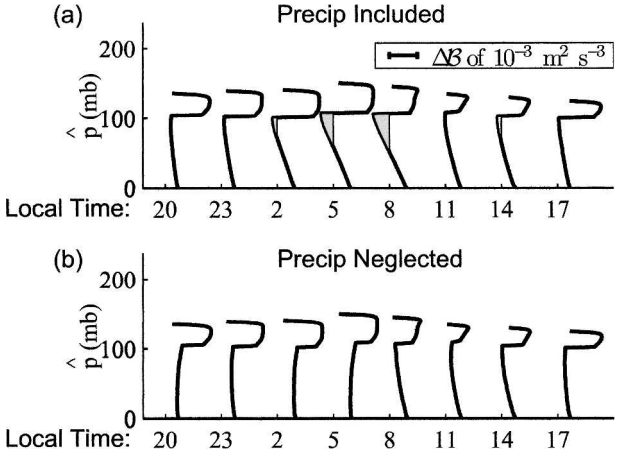

FIG. 8. Diurnally composited buoyancy flux profiles (a) including and (b) excluding the precipitation flux contribution. The tick mark above each time indicates the line of zero $\mathcal{B}$ for that time; regions of negative buoyancy flux are shaded. A sense of the magnitude of $\mathcal{B}$ may be obtained from the scale in the upper-left corner of (a).

the result of strong longwave cooling at cloud top and the daytime minimum is the result of this cooling being canceled by shortwave heating. A related feature is the diurnal variation in the subcloud buoyancy flux minimum. Figure 8a shows substantial negative $\mathcal{B}$ building up below the cloud before sunrise and persisting throughout the morning. The existence of negative buoyancy fluxes during the day is an expected consequence of shortwave heating in the cloud. However, subcloud buoyancy flux becomes negative before dawn and reaches a minimum before 0800 LT, earlier than expected for a BL dominated by shortwave heating.

Figure 8b suggests that the process responsible for these features is the evaporation of drizzle. This graphic shows the results of a sensitivity study in which the buoyancy flux has been recalculated with F_p set to zero. While changing the drizzle rate should, in reality, affect cloud thickness, BL depth, and other aspects of BL structure that would themselves affect the buoyancy flux profiles, this figure is useful as an illustration that drizzle is important to BL structure. In this graphic, we see that without drizzle the time of minimum buoyancy flux is around noon and that cloud-base buoyancy fluxes never become negative. Because significant negative $\mathcal{B}$ leads to BL decoupling (Bretherton and Wyant 1997; Stevens 2000), this suggests that drizzle may be contributing to partial early morning BL decoupling. This hypothesis may be investigated by examining the ability of the lifting condensation level (LCL) derived from shipboard measurements to predict cloud base over the course of a day. In a well-mixed BL, surface and cloud-base humidity are homogenized by mixing, so the surface LCL will be a good predictor of the actual cloud base. In practice, a correction must be applied to the surface LCL to account for the moisture and temperature gradients within the surface layer. By comparing the average surface LCL to that computed from the sondes at 100 m above the surface, we calculate the surface layer to cause an approximately −15 mb bias to the surface LCL. This is consistent with the correction one would make using the observed air–sea moisture differences and assuming a log layer between the 15-m measurement height and 100 m. Figure 9 compares the 6-day mean diurnal cycle of surface LCL (shifted up 15 mb) and the ceilometer-measured cloud base. This figure shows that the BL is more well mixed during the night (though even then there is a slight residual moisture stratification), but rapidly becomes less so in the early morning and remains less well mixed throughout the daylight hours. This phasing corresponds closely to the onset of negative buoyancy flux presented in Fig. 8, corroborating the role of early morning drizzle and later solar absorption in inhibiting efficient vertical mixing of the BL. Figure 8b is also worthwhile as a consistency check on our drizzle fluxes since this graphic shows that a BL with negligibly small drizzle rates would be better mixed than we observe, and thus that the true drizzle rate cannot be too much lower than our estimates.

The stratification apparent in Fig. 9 is not entirely surprising. Previous studies (Albrecht et al. 1995b; Klein et al. 1995; Coakley et al. 2000) support the notion that deeper BLs tend to be more decoupled. This feature is illustrated in Fig. 10, which compares q_v profiles from various campaigns. In this graphic, deeper inversions tend to be associated with stronger BL moisture gradients. The Atlantic Stratocumulus Experiment

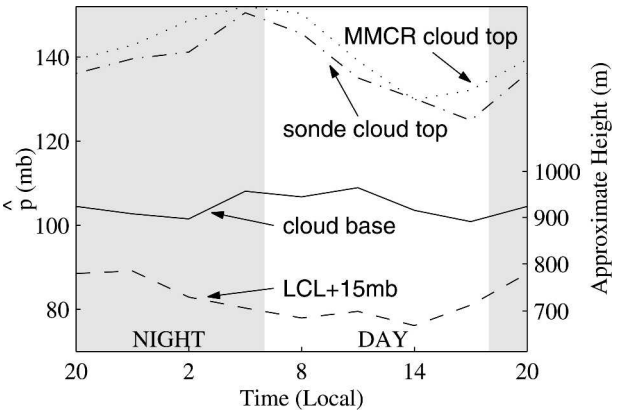

FIG. 9. Comparison between the diurnal cycle of cloud base and that of the LCL. LCL values are shifted up 15 mb to account for the effect of the surface layer. Also shown are $\hat{p}_i$ values diagnosed from radiosonde and from radar.

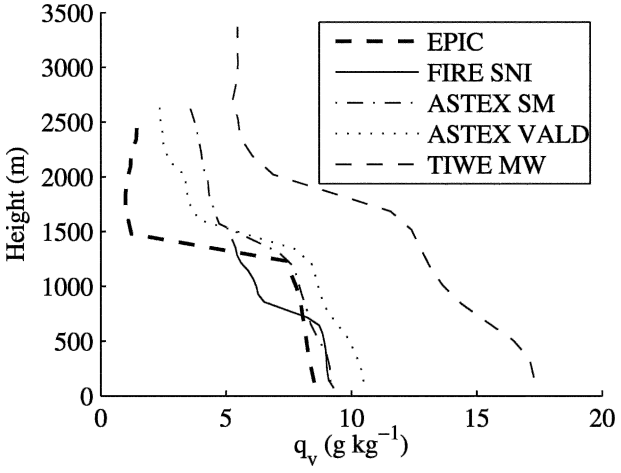

FIG. 10. Comparison of EPIC composite q_v profile with similar profiles from San Nicholas Island (33°N, 119°W), Santa Maria Island (37°N, 25°W), the R/V *Valdivia* (28°N, 24°W), and the R/V *Moana Wave* (0°, 140°W). With the exception of EPIC, these datasets are described in Albrecht et al. (1995b).

(ASTEX) profiles are interesting because they have roughly the same BL depth as EPIC, but show much *more* decoupling, with a scud-capped surface moist layer detraining into thin, patchy stratocumulus near the BL top (Albrecht et al. 1995a). Better mixing in the EPIC region may be related to the presence of a stronger inversion in this area, although this relationship is the subject of ongoing investigation. The fact that no scud was observed during the 6 days of study, and that BL gradients in θ and q_t were found to be quite weak (as discussed in section 1) indicate that even during the day, mixing was sufficient to justify use of the mixed-layer assumption in calculating buoyancy flux profiles.

d. Entrainment parameterization

Conceptually, entrainment results when large eddies penetrate the inversion capping the BL, lose momentum, and fall back through the inversion, drawing filaments of free-tropospheric air back down with them (Turner 1973). As such, many entrainment parameterizations have tended to focus on quantifying the strength of these eddies and the efficiency with which they entrain the overlying air. In a cloud-free convectively driven BL the relation

$$\frac{w_e}{w_*} = A\mathrm{Ri}^{-1} \tag{16}$$

was found to hold well with w_* as defined in (11), bulk Richardson number $\mathrm{Ri} = \Delta b z_i / w_*^2$ (where the inversion density jump Δb is expressed in buoyancy units) and empirically derived entrainment efficiency rate $A \approx 0.2$ (Driedonks 1982; Deardorff 1983). In the presence of cloud, however, (16) ceases to fit the data as written. In this regime, values of A between 1 and 5 have been inferred from aircraft observations (mostly during daytime), with considerable spread between experiments (Nicholls and Turton 1986; de Roode and Duynkerke 1997; Faloona et al. 2005). Such inferences are complicated by the possibility of decoupling, which could result in the appropriate vertical eddy scale being smaller than z_i and thus overpredicting A [since overpredicting z_i would cause an overprediction of Ri, resulting in an overestimation of A in (16)]. The composite diurnal cycle of w_e and w_* inferred from the EPIC data is consistent with this hypothesis. Figure 11 compares the relation between w_e and $w_*\mathrm{Ri}^{-1}$ for the eight samples of the EPIC diurnal cycle with measurements from previous campaigns. The EPIC data support an A value of 1.1, which is in line with the recent Second Dynamics and Chemistry of Marine Stratocumulus (DYCOMS II) field study findings but smaller than suggested by other, earlier experiments. The spread between experiments underscores the considerable uncertainty involved in this calculation. Also, the "×" corresponding to 1100 LT does not fall on the best-fit line

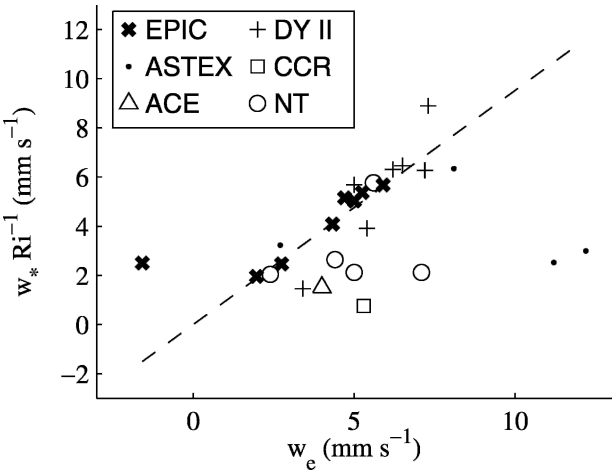

FIG. 11. Comparison of entrainment efficiency from various campaigns. The dashed line is the best fit to the EPIC data (constrained to pass through the origin). The reciprocal of this slope is the best-fit estimate of A. In this diagram, DYII is from DYCOMS II (Faloona et al. 2005) and uses dimethyl sulfide (DMS)-based w_e from their Fig. 5, and w_* and Ri from their Fig. 7. ASTEX uses w_* and Ri from their Table 2 (flights 1–4 only), and w_e from Fig. 12 of de Roode and Duynkerke (1997). Caughey et al. 1982, hereafter CCR) use w_* and Ri from their Eq. (7) and w_e from Roach et al. (1982). Aersol Characterization Experiment (ACE) data are from Boers et al. (1998), which lists w_e and w_*, but yields Ri only after considerable estimation (using their Figs. 5 and 6). NT refers to Nicholls and Turton (1986) and is directly from their Table 1. Note that NT uses Ri with z_i replaced by a (smaller) mixed-layer depth.

because the entrainment inferred for this time is negative—an unphysical prediction. Further, entrainment from the mass budget is used both as the independent variable and in the w_* calculation, which could bias the results. Sensitivity calculations indicate that our estimated uncertainty in entrainment (about 25%) results in an uncertainty in A of around 50%. Finally, the mixed-layer assumption is employed here for all times of day in calculating w_*, even though Fig. 9 suggests that the well-mixed assumption is not perfectly satisfied during daylight hours.

Measurement uncertainty alone, however, is unlikely to account for the wide spread in A reported in the literature. There is no reason A should be a universal constant in cloud-topped mixed layers. Clouds affect turbulence (and thus, perhaps, entrainment) in a multitude of ways, which could depend on environmental conditions in a manner not captured by (16) with A held constant. Choosing which of these processes are important and finding a way to include these processes in a parameterization is at the heart of the current entrainment debate.

We now compare our observations with the predictions of a few recent parameterizations, each of which emphasizes a different cloud process for diagnosing entrainment. The first of these schemes was proposed by Turton and Nicholls (1987). This scheme, hereafter denoted TN, accounts for the enhancement of turbulence by evaporative cooling at cloud top by replacing Δb in (16) with

$$\Delta b_{\mathrm{TN}} = \frac{\Delta b}{1 + a_2\left(1 - \dfrac{\Delta m}{\Delta b}\right)},$$

where $\Delta m = 2\int_0^1 \Delta b(\chi)\, d\chi$. Here, $\Delta b(\chi)$ is the cloud-top buoyancy jump (including evaporative cooling) caused by mixing χ parts inversion-top air with $1 - \chi$ parts cloudy air so that Δm is proportional to the average evaporative buoyancy enhancement over all possible mixtures. Turton and Nicholls found $a_2 = 60$ to fit their data well, although a recent regional model simulation of subtropical stratocumulus suggests that $a_2 = 15$ provides better results when this scheme is implemented within a BL-turbulence parameterization. (McCaa and Bretherton 2004). Entrainment predictions using both values are considered here. A value for A of 0.2 is assumed for this scheme.

The second parameterization comes from Lilly (2002a). This proposal (hereafter DL) also accounts for cloud-top evaporation, this time by replacing Δb in (16) with $\Delta b_{\mathrm{DL}} = \alpha\Delta_{\mathrm{sat}}b + (1 - \alpha)\Delta_b$, where $\Delta_{\mathrm{sat}}b$ is the buoyancy jump across cloud top assuming the above-cloud-top air is saturated. This correction was designed to fit Lilly's observation that cloud-top dynamics seem to be a combination of the values predicted independently for saturated and dry microphysics. The optimal combination of the two cases was chosen empirically to be $\alpha = \tanh(2.45m_*)/\tanh(2.45)$, where m_* is the mixing fraction sufficient to just evaporate the cloud. The other interesting feature of the DL scheme is that turbulence generated at cloud top is weighted more heavily than that generated at the surface by replacing w_* in (16) with $w_{*,\mathrm{DL}} = [3\int_0^{z_i} (z/z_i)\mathcal{B}\, dz]^{1/3}$. For this scheme, we adopt the suggested A of 3.0.

Finally, we consider the parameterization in Lewellen and Lewellen (1998, hereafter LL), which is based on the rather different hypothesis that entrainment is controlled by large-eddy energetics. Here LL assume that a fixed fraction of the turbulent kinetic energy (TKE) generated in the absence of entrainment is depleted through entrainment mixing of buoyant air from the inversion down into the BL. Assuming once again that buoyancy flux is the main source of TKE, the LL parameterization may be written as

$$\eta = \int_0^{z_i} [\mathcal{B}_{\mathrm{NE}} - \mathcal{B}]\, dz \Big/ \int_0^{z_i} \mathcal{B}_{\mathrm{NE}}\, dz,$$

where η is taken as 0.35 on the basis of large-eddy simulations and $\mathcal{B}_{\mathrm{NE}}$ is the buoyancy flux in the absence of entrainment. They also include a correction for radiative cooling in the inversion layer that we omit on the basis that it is not clear how this value should be calculated from the EPIC data, or whether it is even physically relevant (Lilly 2002b). Other parameterizations could be tested against our data; we selected these three because the comparison is straightforward yet the parameterizations are still fairly different.

A comparison of these parameterizations is presented in Fig. 12. Except for the TN parameterization with $a_2 = 60$, all of the schemes agree closely with each other and quite well with the EPIC data. The agreement between the three parameterizations is remarkable, especially since the LL closure completely neglects evaporative enhancement, which plays an essential role in the other two closures. These schemes performed similarly well in a comparison with entrainment observations from the first research flight of DYCOMS II (Stevens et al. 2003). Successful simulation of the entrainment rates from EPIC is impressive because it implies that the closures exhibit the proper sensitivity to the diurnal cycle. Like most other studies, however, our comparison involves large uncertainties. Longer-term measurements similar to those made in EPIC would be extremely useful for reducing these errors.

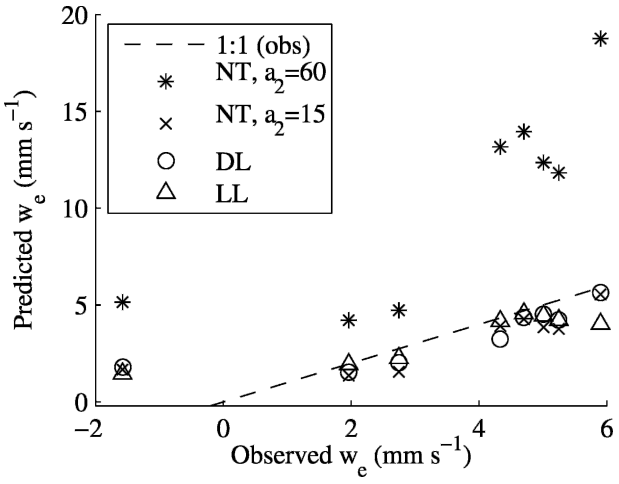

FIG. 12. Entrainment rates predicted by the various schemes for each of the 8 times of day plotted against the observed entrainment rate. The 1:1 line (dashed) depicts perfect agreement with the observations.

5. Conclusions

A clean diurnal cycle sampled by an extensive set of shipborne measurements during EPIC 2001 has provided an excellent opportunity to study the diurnally varying mass, heat, and water budgets of the SE Pacific stratocumulus region and their implications for entrainment and decoupling. We have combined frequent radiosonde observations, ship-based remote sensing of cloud properties, a radiative transfer model, and surface turbulent flux measurements with ECMWF and NCEP analyses of subsidence and horizontal advection to evaluate all terms in these budgets during a 6-day period. The mean budgets over this period showed balances expected for stratocumulus. The diurnal variation of entrainment and the associated warming and drying were balanced by diurnal variations in storage and in the absorption of insolation. Each budget provided an independent estimate of the diurnal cycle of entrainment rate as a budget residual. All three estimates have similar daily means and a consistent diurnal cycle. This cycle consists of fairly constant entrainment rates of 5 mm s^{-1} throughout the night, dropping to near zero by midday before recovering in the evening for a daily mean value of 4 mm s^{-1}.

Buoyancy flux profiles inferred from this analysis show that drizzle, which is negligible in terms of its direct effect on the water and energy budgets (because it largely evaporates before reaching the surface), nonetheless exerts a strong influence on BL dynamics by limiting turbulent mixing below cloud base and thereby promoting decoupling. Independent evidence of partial decoupling is found in the form of increased LCL–cloud-base difference from early morning to late afternoon, although even then residual mixing keeps BL internal gradients of conserved variables relatively small so a mixed-layer approximation is still reasonable. The buoyancy flux profiles are used to test selected entrainment closures, which performed surprisingly well in predicting the correct diurnal cycle of entrainment. That such an internally consistent picture of entrainment into a stratocumulus-capped mixed layer could be obtained from ship-based observations alone is quite remarkable, and is a testament to the suite of ship-based measurements made during EPIC. Coordination of a similar set of measurements with an airborne field campaign could better test this approach and further advance our understanding of the interplay between entrainment, turbulence, drizzle, and the diurnal cycle in stratocumulus.

Acknowledgments. The authors wish to thank Martin Köhler for use of the ECMWF analyses and Hua-Lu Pan and Steve Krueger for the NCEP data. We are also grateful to Christopher Fairall, Taneil Uttal, and Duane Hazen of NOAA/ETL for providing MMCR data and information, and to the crew of the NOAA *RHB* for their assistance during the EPIC cruise. This research was funded by NSF Grant ATM0082384 and NASA Grant NAGS-10624.

APPENDIX

Derivation of Budget Equations

For some quantity A, the time tendency of A can be written in terms of the convergence of its flux F_A:

$$\frac{\partial A}{\partial t} + \mathbf{v} \cdot \boldsymbol{\nabla}_h A + w \frac{\partial A}{\partial z} = -\frac{1}{\rho} \boldsymbol{\nabla} \cdot F_A, \qquad \text{(A1)}$$

where $\boldsymbol{\nabla}_h$ is the horizontal divergence operator (the vertical divergence is considered explicitly) and ρ is the air density. The large-scale pressure field is in hydrostatic balance and by classical Boussinesq scaling assumptions, horizontal pressure perturbations are negligibly small compared to those in the vertical, so at any $\hat{p}$ (defined in section 2a of the text), $\partial\hat{p} = \rho g \partial z$, and by extension the vertical pressure–velocity $\hat{\omega}$ satisfies $\hat{\omega} = \rho g w$. Applying this relation to (A1) results in the following:

$$\frac{\partial A}{\partial t} + \mathbf{v} \cdot \boldsymbol{\nabla}_h A + \hat{\omega} \frac{\partial A}{\partial \hat{p}} = -\frac{1}{\rho} \boldsymbol{\nabla}_h \cdot F_A - g \frac{\partial F_A}{\partial \hat{p}}. \qquad \text{(A2)}$$

Reynolds averaging this last equation and noting that conservation of mass implies $\partial u/\partial x + \partial v/\partial y + \partial\hat{\omega}/\partial\hat{p} = 0$,

$$\frac{\partial \overline{A}}{\partial t} + \overline{\mathbf{v}} \cdot \nabla_h \overline{A} + \hat{\omega}_s \frac{\partial \overline{A}}{\partial \hat{p}} + \frac{\partial \overline{\hat{\omega}' A'}}{\partial \hat{p}} = -g \frac{\partial \overline{F}_A}{\partial \hat{p}}, \quad \text{(A3)}$$

where overbars denote horizontally averaged quantities, primes imply perturbations from this average, and it is recognized that $\overline{\hat{\omega}}$ is the subsidence rate, $\hat{\omega}_s$. In this equation, $\nabla_h \cdot \overline{\hat{\omega}' A'}$ and $\nabla_h \cdot \overline{F}_A$ have been neglected in recognition of their relative insignificance when compared to the vertical gradients. Integrating over the BL depth $\hat{p}_i$, (A3) becomes

$$\int_0^{\hat{p}_i} \frac{\partial \overline{A}}{\partial t} d\hat{p} + \hat{p}_i \langle \overline{\mathbf{v}} \cdot \nabla_h \overline{A} \rangle + \int_0^{\hat{p}_i} \hat{\omega}_s \frac{\partial \overline{A}}{\partial \hat{p}} d\hat{p} + \overline{\hat{\omega}' A'}|_0^{\hat{p}_i} = -g F_A|_0^{\hat{p}_i}, \quad \text{(A4)}$$

where angle brackets refer to BL-averaged quantities. The first term in (A4) can be simplified by noting that

$$\int_0^{\hat{p}_i} \frac{\partial \overline{A}}{\partial t} d\hat{p} = \frac{\partial}{\partial t} \int_0^{\hat{p}_i} \overline{A}\, d\hat{p} - \frac{\partial \hat{p}_i}{\partial t} \overline{A}|_{\hat{p}_i -}, \quad \text{(A5)}$$

$$= \frac{\partial (\hat{p}_i \langle \overline{A} \rangle)}{\partial t} - \frac{\partial \hat{p}_i}{\partial t} \overline{A}|\hat{p}_{i-}, \quad \text{(A6)}$$

$$= [\langle \overline{A} \rangle - \overline{A}|_{\hat{p}_i -}] \frac{\partial \hat{p}_i}{\partial t} + \hat{p}_i \frac{\partial \overline{A}}{\partial t}, \quad \text{(A7)}$$

where $\overline{A}|_{\hat{p}_i -}$ is $\overline{A}$ evaluated just below the inversion. The third term in (A4) may be rewritten as

$$\int_0^{\hat{p}_i} \hat{\omega}_s \frac{\partial \overline{A}}{\partial \hat{p}} d\hat{p} = \int_0^{\hat{p}_i} \frac{\partial (\hat{\omega}_s \overline{A})}{\partial \hat{p}} d\hat{p} - \int_0^{\hat{p}_i} \overline{A} \frac{\partial \hat{\omega}_s}{\partial \hat{p}} d\hat{p}, \quad \text{(A8)}$$

$$= \hat{\omega}_s \overline{A}|_{\hat{p}_i -} - \frac{\partial \hat{\omega}_s}{\partial \hat{p}} \hat{p}_i \langle \overline{A} \rangle, \quad \text{(A9)}$$

$$= \hat{\omega}_s [\overline{A}|_{\hat{p}_i -} - \langle \overline{A} \rangle]. \quad \text{(A10)}$$

In the above equation, the second equality follows from assuming that horizontal divergence, $-\partial \hat{\omega}_s / \partial \hat{p}$, is constant in height (true for a well-mixed BL since in this case horizontal winds are height independent) and noting that $\hat{\omega}_s = 0$ at the surface. The final line results from noting that if $\partial \hat{\omega}_s / \partial \hat{p}$ is height independent, then $\hat{p}_i \partial \hat{\omega}_s / \partial \hat{p} = \hat{\omega}_s|_{\hat{p}_i}$.

Applying (A7) and (A10) to (A4) and noting that turbulent flux across the cloud top is predominantly due to entrainment of above-BL air, a relationship expressed by $\overline{\hat{\omega}' A'}|_{\hat{p}_i} = -\hat{\omega}_e (\overline{A}|_{\hat{p}_i +} - \overline{A}|_{\hat{p}_i -})$ (where $\hat{\omega}_e$ is the pressure–entrainment rate):

$$\hat{p}_i \left[\frac{\partial \overline{A}}{\partial t} + \langle \overline{\mathbf{v}} \cdot \nabla_h \overline{A} \rangle \right] + \left(\hat{\omega}_s - \frac{\partial \hat{p}_i}{\partial t} + \hat{\omega}_e \right) [\overline{A}|_{\hat{p}_i -} - \langle \overline{A} \rangle] - \hat{\omega}_e [\overline{A}|_{\hat{p}_i +} - \langle A \rangle] - \overline{\hat{\omega}' A'}|_0 + g F_A|_0^{\hat{p}_i} = 0. \quad \text{(A11)}$$

Defining $\Delta A = [\overline{A}|_{\hat{p}_i +} - \langle A \rangle]$ (where $\overline{A}|_{\hat{p}_i +}$ is $\overline{A}$ evaluated just above the inversion) and noting that $\hat{\omega}_s - (\partial \hat{p}_i / \partial t) + \hat{\omega}_e = \overline{\mathbf{v}} \cdot \nabla_h \hat{p}_i$ [from (3)],

$$\hat{p}_i \left[\frac{\partial \overline{A}}{\partial t} + \langle \overline{\mathbf{v}} \cdot \nabla_h \overline{A} \rangle \right] - \overline{\hat{\omega}' A'}|_0 + g F_A|_0^{\hat{p}_i} - \hat{\omega}_e \Delta A = [\langle A \rangle - \overline{A}|_{\hat{p}_i -}] \overline{\mathbf{v}} \cdot \nabla_h \hat{p}_i, \quad \text{(A12)}$$

which yields the budget equations presented in this study [(1) and (2)] when $\overline{A}$ is replaced by q_t [which makes the turbulent surface flux $g \cdot (\mathrm{LHF}/L)$ and the flux function $F_{q_t} = F_P$] or by s_l (in which case $\overline{\hat{\omega}' A'}|_0 = g \cdot \mathrm{SHF}$ and $F_{s_l} = F_R - L F_P$).

REFERENCES

Albrecht, B. A., C. W. Fairall, D. W. Thomson, A. B. White, J. B. Snider, and S. Nicholls, 1990: Surface-based remote-sensing of the observed and the adiabatic liquid water-content of stratocumulus clouds. *Geophys. Res. Lett.,* **17,** 89–92.

——, C. S. Bretherton, D. Johnson, W. H. Scubert, and A. S. Frisch, 1995a: The Atlantic Stratocumulus Transition Experiment—ASTEX. *Bull. Amer. Meteor. Soc.,* **76,** 889–904.

——, M. P. Jenson, and W. J. Syrett, 1995b: Marine boundary layer structure and fractional cloudiness. *J. Geophys. Res.,* **100,** 14 209–14 222.

Boers, R., K. B. Krummel, S. T. Siems, and G. D. Hess, 1998: Thermodynamic structure and entrainment of stratocumulus over the southern ocean. *J. Geophys. Res.,* **103,** 16 637–16 650.

Bretherton, C. S., and M. C. Wyant, 1997: Moisture transport, lower-tropospheric stability, and decoupling of cloud-topped boundary layers. *J. Atmos. Sci.,* **54,** 148–167.

——, T. Uttal, C. W. Fairall, S. E. Yuter, R. A. Weller, D. Baumgardner, K. Comstock, and R. Wood, 2004: The EPIC 2001 stratocumulus study. *Bull. Amer. Meteor. Soc.,* **85,** 967–977.

Brost, R. A., J. C. Wyngaard, and D. H. Lenschow, 1982: Marine stratocumulus layers. Part II: Turbulence budgets. *J. Atmos. Sci.,* **39,** 818–836.

Caughey, S., B. Crease, and W. Roach, 1982: A field study of nocturnal stratocumulus. II: Turbulence structure and entrainment. *Quart. J. Roy. Meteor. Soc.,* **108,** 125–144.

Coakley, J. A., and Coauthors, 2000: The appearance and disappearance of ship tracks on large spatial scales. *J. Atmos. Sci.,* **57,** 2765–2778.

Comstock, K., R. Wood, S. E. Yuter, and C. S. Bretherton, 2004: Reflectivity and rain rate in and below drizzling stratocumulus. *Quart. J. Roy. Meteor. Soc.,* **130,** 2891–2918.

Deardorff, J., 1983: A multi-limit mixed-layer entrainment formulation. *J. Phys. Oceanogr.,* **13,** 988–1002.

de Roode, S. R., and P. G. Duynkerke, 1997: Observed Lagrangian transition of stratocumulus into cumulus during ASTEX: Mean state and turbulence structure. *J. Atmos. Sci.,* **54,** 2157–2173.

Dong, X., and G. G. Mace, 2003: Arctic stratus cloud properties and radiative forcing derived from ground-based data collected at Barrow, Alaska. *J. Climate,* **16,** 445–460.

Driedonks, A., 1982: Models and observations of the growth of the atmospheric boundary layer. *Bound.-Layer Meteor.,* **23,** 283–306.

Duynkerke, P. G., and J. Teixeira, 2001: Comparison of the

ECMWF reanalysis with FIRE I observations: Diurnal variation of marine stratocumulus. *J. Climate,* **14,** 1466–1478.

Fairall, C. W., E. F. Bradley, D. P. Rogers, J. B. Edson, and G. S. Young, 1996: Bulk parameterization of air-sea fluxes for Tropical Ocean Global Atmosphere Coupled Ocean Atmosphere Response Experiment. *J. Geophys. Res.,* **101C,** 3747–3764.

Faloona, I., and Coauthors, 2005: Observations of entrainment in eastern Pacific marine stratocumulus using three conserved scalars. *J. Atmos. Sci.,* **62,** 3268–3285.

Garreaud, R. D., and R. Muñoz, 2004: The diurnal cycle in circulation and cloudiness over the subtropical southeast Pacific: A modeling study. *J. Climate,* **17,** 1699–1710.

Hartmann, D. L., M. E. Ockert-Bell, and M. L. Michelson, 1992: The effect of cloud type on earth's energy balance: Global analysis. *J. Climate,* **5,** 1281–1304.

Hignett, P., 1991: Observations of diurnal variation in a cloud-capped marine boundary layer. *J. Atmos. Sci.,* **48,** 1474–1482.

Hogg, D. C., F. O. Guiraud, J. B. Snider, M. T. Decker, and E. R. Westwater, 1983: A steerable dual-channel microwave radiometer for measurement of water vapor and liquid in the troposphere. *J. Climate Appl. Meteor.,* **22,** 789–806.

Klein, S. A., and D. L. Hartmann, 1993: The seasonal cycle of low stratiform clouds. *J. Climate,* **6,** 1587–1606.

——, ——, and J. R. Norris, 1995: On the relationships among low-cloud structure, sea surface temperature, and atmospheric circulation in the summertime Northeast Pacific. *J. Climate,* **8,** 1140–1155.

Lenschow, D. H., M. Y. Zhou, L. S. Chen, and X. D. Xu, 2000: Measurements of fine-scale structure at the top of marine stratocumulus. *Bound.-Layer Meteor.,* **97,** 331–357.

Lewellen, D., and W. Lewellen, 1998: Large-eddy boundary layer entrainment. *J. Atmos. Sci.,* **55,** 2645–2665.

Lilly, D., 1968: Models of cloud-topped mixed layers under a strong inversion. *Quart. J. Roy. Meteor. Soc.,* **94,** 292–309.

——, 2002a: Entrainment into mixed layers. Part I: Sharp-edged and smoothed tops. *J. Atmos. Sci.,* **59,** 3340–3352.

——, 2002b: Entrainment into mixed layers. Part II: A new closure. *J. Atmos. Sci.,* **59,** 3353–3361.

Martin, G. M., W. Johnson, and A. Spice, 1994: The measurement and parameterization of effective radius of droplets in warm stratocumulus clouds. *J. Atmos. Sci.,* **51,** 1823–1842.

McCaa, J., and C. Bretherton, 2004: A new parameterization for shallow cumulus convection and its application to marine subtropical cloud-topped boundary layers. Part II: Regional simulations of marine boundary layer clouds. *Mon. Wea. Rev.,* **132,** 883–896.

McClatchey, R., R. Fenn, J. Selby, F. Volz, and J. Garing, 1972: Optical properties of the atmosphere. Tech. Rep. AFCRL-72-0497, Air Force Cambridge Research Lab., Hanscom AFB, Bedford, MA, 108 pp.

McNoldy, B., P. E. Ciesielski, W. H. Schubert, and R. H. Johnson, 2004: Surface winds, divergence, and vorticity in stratocumulus regions using Quikscat and reanalysis. *Geophys. Res. Lett.,* **31,** L08105, doi:10.1029/2004GL019768.

Nicholls, S., 1984: The dynamics of stratocumulus: Aircraft observations and comparisons with a mixed layer model. *Quart. J. Roy. Meteor. Soc.,* **110,** 783–820.

——, and J. Leighton, 1986: An observational study of the structure of stratiform cloud sheets: Part I. Structure. *Quart. J. Roy. Meteor. Soc.,* **112,** 431–460.

——, and J. Turton, 1986: An observational study of the structure of stratiform cloud sheets: Part II. Entrainment. *Quart. J. Roy. Meteor. Soc.,* **112,** 461–480.

Randall, D., 1980: Conditional instability of the first kind upside-down. *J. Atmos. Sci.,* **37,** 125–130.

——, and Coauthors, 2003: Confronting models with data: The GEWEX cloud systems study. *Bull. Amer. Meteor. Soc.,* **84,** 455–469.

Roach, W. T., R. Brown, S. J. Caughey, B. A. Crease, and A. Slingo, 1982: A field study of nocturnal stratocumulus: I. Mean structure and budgets. *Quart. J. Roy. Meteor. Soc.,* **108,** 103–123.

Rozendaal, M. A., C. B. Leovy, and S. A. Klein, 1995: An observational study of diurnal variations of marine stratiform cloud. *J. Climate,* **8,** 1795–1809.

Schubert, W. H., J. S. Wakefield, E. J. Steiner, and S. K. Cox, 1979: Marine stratocumulus convection. Part I: Governing equations and horizontally homogenous solutions. *J. Atmos. Sci.,* **36,** 1286–1307.

Stephens, G. L., P. M. Gabriel, and P. T. Partain, 2001: Parameterization of atmospheric radiative transfer. Part I: Validity of simple models. *J. Atmos. Sci.,* **58,** 3391–3409.

Stevens, B., 2000: Cloud transitions and decoupling in shear-free stratocumulus-topped boundary layers. *Geophys. Res. Lett.,* **27,** 2557–2560.

——, 2002: Entrainment in stratocumulus-topped mixed layers. *Quart. J. Roy. Meteor. Soc.,* **128,** 2663–2689.

——, and Coauthors, 2003: On entrainment rates in nocturnal marine stratocumulus. *Quart. J. Roy. Meteor. Soc.,* **129,** 3469–3493.

Turner, J., 1973: *Buoyancy Effects in Fluids.* Cambridge Press, 360 pp.

Turton, J., and S. Nicholls, 1987: A study of the diurnal variation of stratocumulus using a multiple mixed layer model. *Quart. J. Roy. Meteor. Soc.,* **113,** 969–1009.

Weare, B., 1996: Evaluation of the vertical structure of zonally averaged cloudiness and its variability in the Atmospheric Model Intercomparison Project. *J. Climate,* **9,** 3419–3431.

Wood, R., and J. P. Taylor, 2001: Liquid water path variability in unbroken marine stratocumulus. *Quart. J. Roy. Meteor. Soc.,* **127,** 2635–2662.

——, and C. S. Bretherton, 2004: Boundary layer depth, entrainment, and decoupling in the cloud-capped subtropical and tropical marine boundary layer. *J. Climate,* **17,** 3576–3588.

——, ——, and D. L. Hartmann, 2002: Diurnal cycle of liquid water path over the subtropical and tropical oceans. *Geophys. Res. Lett.,* **29,** 2092, doi:10.1029/2002GL015371.